Received: 7 February 2024 | Revised: 29 July 2024 | Accepted: 22 August 2024 | Published online: 13 September 2024

RESEARCH ARTICLE

Journal of Optics and Photonics Research
2025, Vol. 2(2) 93–103
DOI: 10.47852/bonviewJOPR42022592

Study of Combustion-Derived Monoclinic Crystal ($Ba_2MgSi_2O_7$) Structure and Dy^{3+} Luminescence for Generation of White Long Afterglow Phosphor and Its Applications

Shashank Sharma[1,*] and Sanjay Kumar Dubey[2,*]

[1]*Department of Physics, Government Gramya Bharti College Hardibajar, Korba, India*

[2]*Department of Physics, Dr. Radhabai Government Navin Girls College, Raipur, India*

Abstract: Here, the crystalline structural (X-ray diffraction), morphological (field emission scanning electron microscopy), optical (photoluminescence, Commission International de l'Eclairage, & correlated color temperature), and thermal (thermoluminescence) characteristics of $Ba_2MgSi_2O_7$:Dy^{3+} nanophosphor were investigated. The compounds were successfully prepared by the combustion synthesis technique at 700 °C for 5 min, followed by annealing at 1000 °C for 3 h. X-ray diffraction (XRD) patterns have shown a single-phase material having a monoclinic structure in space group C2/c. The particle morphological shapes have shown in the nanorange. All the kinetic and trapping parameters of the trap center evaluated by the thermoluminescence (TL) glow curve were examined via the Chen empirical formula. The trap depths were found to be in the range of 0.66–0.74 eV. Prominent emission peaks were observed at 474 nm (blue), 572 nm (yellow), and 667 nm (red) due to three optical transitions ($^4F_{9/2} \rightarrow {}^6H_{15/2,\ 13/2,\ 11/2}$), respectively. In our investigation, the critical distance (R_c) is calculated as 16.89 Å; therefore, the mechanism involved in the concentration quenching of $Ba_2MgSi_2O_7$ activated with a 3 mol% concentration of Dy^{3+} ions are considered to be the multipole-multipolar interaction. In photochromatic characterization study, the Commission International de l'Eclairage (CIE) chromaticity coordinates are found in the white color region, and it is well suited for generating cool light emission. The calculated correlated color temperature is 6113 K, and the color rendering index R_a is above 89. The prepared phosphor is potentially applicable for white LED-based solid-state lighting devices and long-persistent phosphor.

Keywords: $Ba_2MgSi_2O_7$:Dy^{3+}, monoclinic, X-ray diffraction, field emission scanning electron microscopy, thermoluminescence, correlated color temperature, color rendering index

1. Introduction

Luminescence covers an extremely wide range of physical processes that have fundamental scientific significance and find wide practical applications. It is rapidly establishing new trends and socially useful innovations. The rare-earth-doped materials show great potential for being used for the development of efficient laser and luminescent media [1]. At the present time, phosphor-converted white light-emitting diodes (w-LEDs) using phosphors to convert the radiation of a near-ultraviolet (UV) or blue LED chip into white light are conferred more considerations [2]. Furthermore, oxygen vacancies in self-activated photoluminescent material, substitution of cations via tunable photoluminescence, different site occupations are the most significant photoluminescence and spectroscopic effects that can be used to precisely determine different characteristics in phosphors for developing w-LEDs. Lighting industries are essentially recognized for their distinct vision for the future due to the rising need and unforeseen popularity of long-persistent phosphors and phosphor-converting w-LEDs. Consequently, they are predicted to be the foreseeable future of solid-state lighting (SSL) devices due to their ease of maintenance. In the near future, w-LEDs are predicted to be a better replacement for conventional fluorescent and incandescent light sources because of their outstanding features, such as energy efficiency, higher luminous efficiency, compactness, flat packaging, dependability, extended longevity, environment protection [3], low energy consumption, and better stability [4], as well as the potentially hazardous mercury-free composition [5] that is occasionally utilized in backlit lamps. Moreover, white LEDs may reduce the consumption of energy for incandescent light bulbs by approximately 70%. The potential benefits and plenty of applications of silicate-based phosphors over sulfide and aluminate phosphors have gained remarkable attention. Due to its various advantages, such as eco-friendly nature, facial synthesis, crystal structure, brightness, high efficiency Si solar cells, green emitters, etc. [6, 7], as well as abundant resources, lower cost,

*Corresponding authors: Shashank Sharma, Department of Physics, Government Gramya Bharti College Hardibajar, Korba, India. Email: shashanksharma1729@gmail.com and Sanjay Kumar Dubey, Department of Physics, Dr. Radhabai Government Navin Girls College, Raipur, India. Email: sanjaydubey2166@gmail.com

superior water resistance, outstanding chemical and thermal stability [8], non-toxic nature, and an array of emission colors spanning blue to yellow. Silicates find an important place in typical low-permittivity ceramic systems due to the covalent features of the silicon-oxygen (Si-O) bond [9]. The crystal structure of the $Ba_2MgSi_2O_7$ host is monoclinic in space group C2/c [10]. SiO_4 and MgO_4 tetrahedral layers in two dimensions are joined by shared corners. Eight oxygen ions collaborate with each other to coordinate both the Ba^{2+} ions also located in layers [11]. The most prevalent way of producing white light emissions, which are utilized in readily accessible LEDs, is down-converting the blue light from an InGaN chip utilizing yellow emitting phosphor materials, especially $Y_3Al_5O_{12}$: Ce^{3+} (YAG : Ce) [12] and $Y_2BaAl_4SiO_{12}$: Ce^{3+} [13]. This particular type of w-LED shows a minimal color rending index (CRI) of less than 80% and a high correlated color temperature (CCT) that exceeds a specific temperature due to red emission deficit [14].

It is indeed conceivable for the combination of blue and yellow light-emitting phosphors to generate white light emission. The dipole transitions having parity allowed for both electric and magnetic transitions that possesses the probability of hyper-transition are responsible for the spectral characteristics of Dy^{3+}-activated compounds [15]. The white light emissions in the dysprosium [Dy^{3+}] ions are caused via the three transitions in visible regions, including $^4F_{9/2} \rightarrow {}^6H_{15/2}$ with strong blue emission (470–500 nm), $^4F_{9/2} \rightarrow {}^6H_{13/2}$ with strong yellow emission (570–600 nm), and $^4F_{9/2} \rightarrow {}^6H_{11/2}$ with weak red emission (600–700 nm), that are commonly observed in dysprosium [Dy^{3+}] ions [16, 17]. There are numerous reports on the study of the dibarium magnesium di silicate structure's luminescent features under UV excitation [10, 11, 15, 18]. It is generally agreed that dysprosium [Dy^{3+}] ions appear to exist in host lattice and can operate effectively as a luminescence center and trap. This is primarily due to the penetration of dysprosium ions into the host crystal lattice site during the doping process and formation of deeper traps. Dy^{3+}-doped mellite compounds have demonstrated their high reliability for phosphors with long persistence behavior. The outstanding efficiency, sharpness, and numerous additional luminescent features of rare-earth ions serve as foundation for the most of these applications [7]. We may use Dy^{3+}-activated $Ba_2MgSi_2O_7$ to prepare inexpensive and eco-friendly w-LEDs. The investigators also found that the phosphor exhibits the optimum intensity at the concentration of 3 mol% dopant ions. This nano crystalline phosphor was prepared by the low temperature conventional combustion synthesis technique. The structural (X-ray diffraction (XRD)), morphological (FESEM), optical (PL), photo chromaticity coordinates (CIE & CCT), and thermal (TL) properties were investigated.

2. Experimental Section

2.1. Combustion synthesis

In the scientific community, many soft-chemical synthesis methods generally include combustion synthesis, sol-gel, co-precipitation, spray pyrolysis, and hydrothermal synthesis, microwave hydrothermal synthesis and deposition from solutions have been efficiently utilized for the production of phosphate-based w-LED phosphors and solid-state materials with minimum use of an expensive high-temperature muffle furnace and pressures. The aforementioned methods essentially require the most liquid substances that can be easily adjusted as well as being completely homogenized. It is well known that nano-sized phosphors can be produced by the combustion synthesis process. Inorganic materials have also prepared by this process to enhance their unique characterizations such as structural, morphological, optical, and thermal properties. Combustion synthesis technique is a quick, easier, having efficient reaction rate, cheaper, time and energy saving method, which include silicates and aluminates. Nanoparticles provide enhanced efficiency in crystalline structure, control over the morphology, homogeneity, and various characteristics of phosphors [11]. Highly sophisticated substances like powder, ceramics, intermetallic, composites, and functional materials are synthesized using this technique [19].

2.2. Chemicals and materials

Ba $(NO_3)_2$. xH_2O (99.99% pure, trace metals basis), Mg $(NO_3)_2$. xH_2O (99.99% pure, trace metals basis), SiO_2. xH_2O (99.99% pure, trace metals basis), Dy $(NO_3)_3$. xH_2O (99.99% pure, trace metals basis), NH_2-CO-NH_2 (Merck Millipore, trace metals basis), and distilled ionized water (99.99% pure, trace metals basis), along with H_3BO_3 (99.99% pure, trace metals basis) were purchased from Sigma-Aldrich & Merck Millipore Corporation and supplied by Mehta Scientific Works Reliable Traders, Vidyanagar, Bilaspur (Chhattisgarh), India. All the starting chemical reagents were used without further purification. A silica crucible (SiO_2, Diameter: 25 mm, Height: 38 mm) and an agate mortar and pestle (diameter: 5") were used in the sintering process of the powder samples. The materials were weighed using a Shimadzu ATX 224 single-pan analytical balance.

2.3. Sample synthesis

As shown in Figure 1, $Ba_2MgSi_2O_7$: Dy^{3+} powder sample with the 3 mol% (Dy^{3+}) dopant was prepared using conventional low temperature combustion synthesis technique. All the precursor materials were used in analytical reagent grade (99.99% pure) form. Urea was utilized as a combustion fuel, and entire metal nitrates were used as an oxidizer [11, 18], along with little amounts of boric acid [H_3BO_3] utilized as flux. All initial ingredients were weighed depending on the stochiometric ratio and mixed homogeneously in agate mortar & pestle (diameter-5") for ~ 2 h to prepare a paste-like solution. After that the entire mixture was conveyed to a silica crucible and stored within a well-maintained programmable muffle furnace at a constant temperature of 700 °C for ~ 5 min. Within 5 mins, the white flame turned into a foamy powder sample. Afterwards, the foamy powder sample was post-annealed at 1000 °C for 3 h, after being reconstituted in a sealed container. The resultant powder sample was examined using XRD, FESEM, PL, TL, and CIE analysis for structural, morphological, optical, thermal, and photo chromaticity characterization studies. For the combustion process, low temperature means the transformation of any material from flame to a foamy powder sample at very temperature (i.e., below 1000 °C). In the present case, the material was transformed from flame to a foamy powder sample at 700 °C temperature.

The following chemical reactions are assumed [18]:

$$Ba\,(NO_3)_2 + Mg(NO_3)_2 + SiO_2 * H_2O + NH_2CONH_2 + H_3BO_3 \rightarrow Ba_2MgSi_2O_7 + Gaseous\ Products\,[H_2O(\uparrow) + CO_2(\uparrow) + N_2(\uparrow)] + Energy \quad (1)$$

Figure 1
Synthesis steps used for Dy^{3+}-activated powder sample

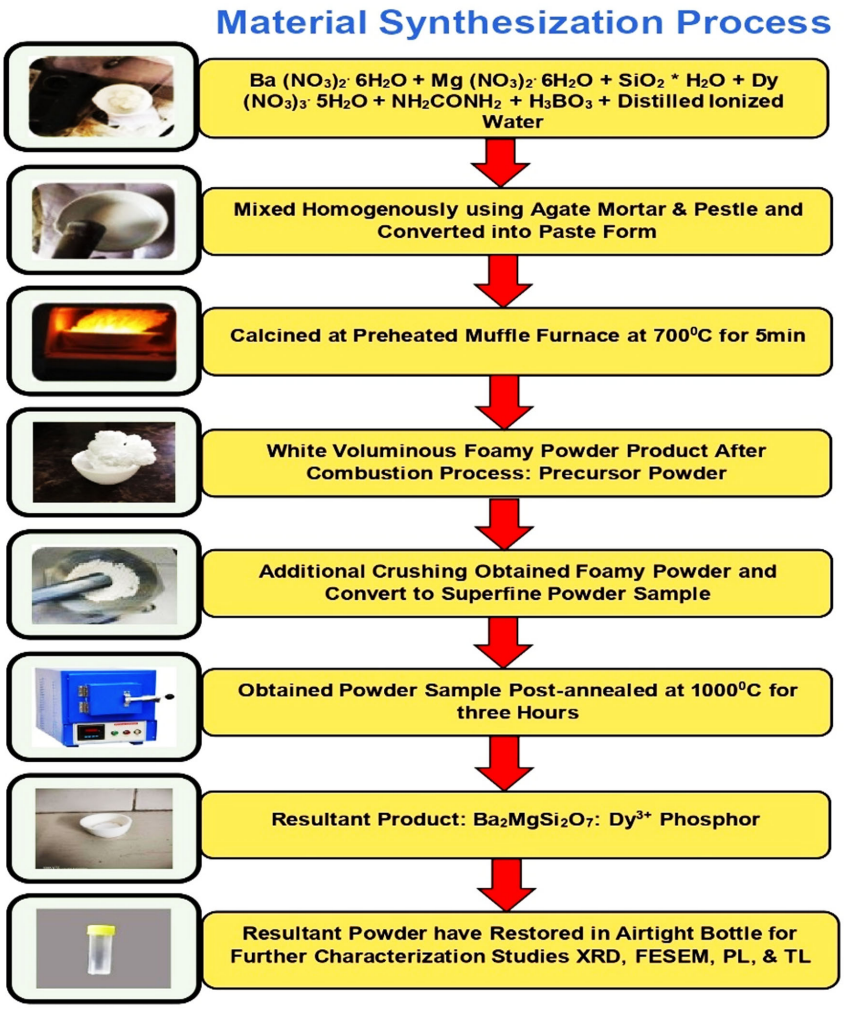

$$Ba(NO_3)_2 + Mg(NO_3)_2 + SiO_2 * H_2O + NH_2CONH_2 + H_3BO_3 + Dy(NO_3)_3 \rightarrow Ba_2MgSi_2O_7 : Dy^{3+} + Gaseous\ Products\,[H_2O(\uparrow) + CO_2(\uparrow) + N_2(\uparrow)] + Energy \quad (2)$$

Entire oxidizing valency/total reducing valency (O/F) is equivalent to one, signifying that the entire combustion process occurs when the greatest amount of energy is liberated. Metal nitrates (oxidizers) and urea (fuel) act as the numerical coefficients to calculate the stoichiometry balance [11]. In addition to determining the kind of fuel, the quantity of fuel has an enormous effect on the substance's morphology, particle size, and specific surface area. Selecting the oxidant/fuel ratio is the most significant step since it determines the chemical composition of the produced nanomaterials. The oxidizer-to-fuel ratio is termed "Ψ", which is defined as follows [20]:

$$\Psi = \frac{\text{total valency of fuel}}{\text{total valency of oxidizer}} \quad (3)$$

2.4. Characterization

For the determination of structural properties, powder diffraction patterns were obtained using a Bruker D8 advance X-ray diffractometer [NIT Raipur, Chhattisgarh] with Cu-K_α radiation ($\lambda = 1.5406$ Å, 40 kV, 40 mA). Particle morphology was analyzed using a ZEISS model [FESEM Centre, NIT Raipur, Chhattisgarh]. Photoluminescence characteristics, including excitation and emission spectra, were analyzed using a Shimadzu RF5301 PC Spectrofluorophotometer (SOS, Department of Physics, Pt. Ravishanker Shukla University, Raipur, Chhattisgarh). TL glow curves were recorded using a Nucleonix (Hyderabad, India) PC-based TLD Reader (TL 1009I) (SOS, Department of Physics, Pt. Ravishanker Shukla University, Raipur, Chhattisgarh).

3. Results and Discussion

3.1. Phase composition

The structural properties of the resultant powder sample were analyzed using the recorded XRD pattern shown in Figure 2. Looking at the diffraction angle axis of the recorded XRD patterns shows that they match well with the standard JCPDS PDF file number #23-0842 [21]. The diffraction angles in the range of 10°–80° were used for calculating the structural data. The crystal structure is monoclinic and contains distinct $[Si_2O_7]^{6-}$ units interconnected via Mg^{2+} ions in tetrahedral coordination and Ba^{2+} ions coordinated by eight O^{2-} ions. The cell parameters are

Figure 2
XRD pattern of Dy^{3+}-activated $Ba_2MgSi_2O_7$ powder sample

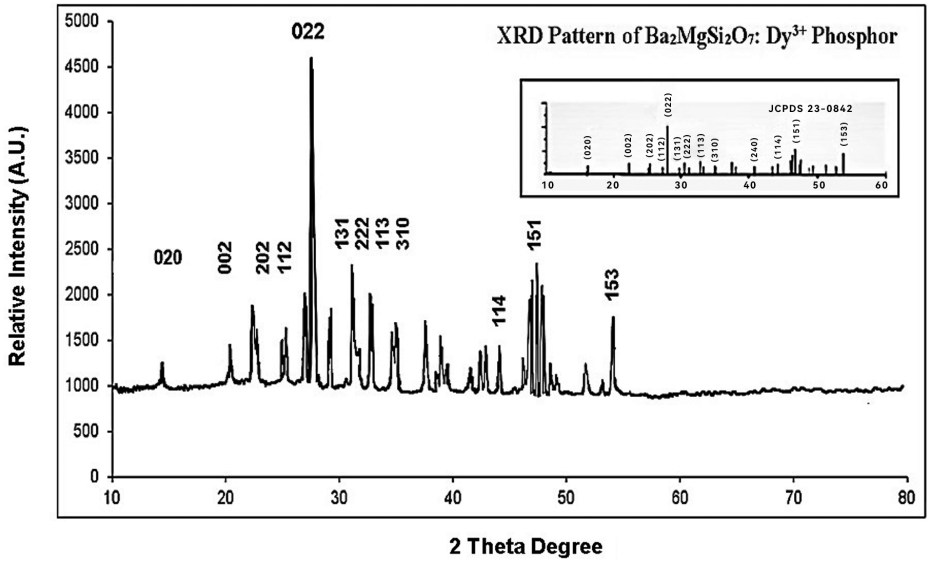

a = 8.4128 Å, b = 10.7101 Å, c = 8.4387 Å, α = 90°, β = 110.71°, and γ = 90° [11, 18], and the unit cell volume is 303.0 (Å)^3. Additionally, the phase composition of the synthesized phosphor sample is shown to be unaffected by doping process. The Ba^{2+} ion positions in the host lattice of $Ba_2MgSi_2O_7$ are anticipated to be occupied by the Dy^{3+} ions, according to similar ion radii. The XRD pattern confirms that the pure monoclinic phase of $Ba_2MgSi_2O_7$ with space group C2/c is formed at the post-annealing temperature of 1000 °C for 3 h.

The XRD patterns indicated a few additional peaks. XRD peaks were peaked at (15.32), (22.44), (25.29), (26.84), (27.51), (29.24), (31.19), (32.67), (34.89), (44.19), (47.37), and (54.21) corresponding to (020), (002), (202), (112), (022), (131), (222), (113), (310), (114), (151), and (153) planes, respectively, and more discerning and distant XRD peaks likewise (2 θ = 22.44 (002), 27.51 (022), 29.24 (131), 31.19 (222), 32.67 (113), 54.21 (153) were selected for crystallite size estimation.

3.1.1. Determination of crystallite/particle size (D)

The Debye-Scherer empirical equation [18, 22] is used to determine the average particle size (D) of the synthesized $Ba_2MgSi_2O_7$: Dy^{3+} phosphor, and the value is ~ 34 nm, as shown in Table 1. It is represented as follows:

$$D = \frac{k\lambda}{\beta Cos\theta} \quad (4)$$

Table 1
Determination of average crystallite size (D)

Diffraction angle	Respective plane	Average crystallite size
22.44	002	32
27.51	022	37
29.24	131	33
31.19	222	34
32.67	113	36
54.21	153	32
Average crystallite size (D)		~34 nm

where k is the Debye-Scherrer constant [0.94], λ is the X-ray wavelength, β is the FWHM (full width half maximum) of the diffraction peak, θ is the diffraction angle, and D is the crystallite size.

We evaluate data with regard to the inter-atomic distance as well as ionic radii from the Shannon's research article [11, 23]. In host crystal lattice ($Ba_2MgSi_2O_7$), dopant [Dy^{3+}] ions are anticipated to substitute Ba^{2+} sites, on the basis that the coordination number of Ba^{2+} ions is eight, and those of Mg^{2+} and Si^{4+} ions are four. It is complicated to incorporate Dy^{3+} ions into tetrahedral [MgO_4] or [SiO_4] sites, but [BaO_8] polyhedron is appropriate. This seems to be primarily because the ionic radius of Dy^{3+} (0.97 Å) is similar to that of Ba^{2+} (1.42 Å). However, we additionally notice that the ionic radii of Mg^{2+} (0.58 Å) and Si^{4+} (0.26 Å) are extremely small. Consequently, Dy^{3+} ions cannot be incorporated into these sites [18].

3.2. FESEM analysis

Phosphor particle morphology, including its shape, size, and imperfections, influences the particle's luminescence characteristics. Nanoparticles have increased in the efficiency of optical & thermal intensity of the phosphor. The FESEM image of the as-prepared $Ba_2MgSi_2O_7$: Dy^{3+} sample morphology is shown in Figure 3 at magnifications of 10.00 KX. The morphological image indicates that the grains consist of several kinds of nanoparticles.

The combustion process releases gases, which cause the agglomerated particles, pore spaces, and voids. The average particle size was determined by counting 100 individual particles from the FESEM image, and the outcome was 37.5 nm. The nano-order has been achieved with a significantly higher degree of consistency in the particle size. Several pieces of literature highlight the effects of particle clustering in different powder products. The high-temperature heat treatment also commonly results in particle agglomeration, which results from small particles clustering by diffusion [24].

3.2.1. Difference between FESEM and XRD analysis

According to several reports, the particle size seen in the FESEM analysis is larger than the crystallite size seen in the XRD analysis. For estimating particle size, FESEM analysis is a more relevant technique compared to XRD analysis. The fundamental concepts and

Figure 3
FESEM image of Dy^{3+}-doped $Ba_2MgSi_2O_7$ powder sample

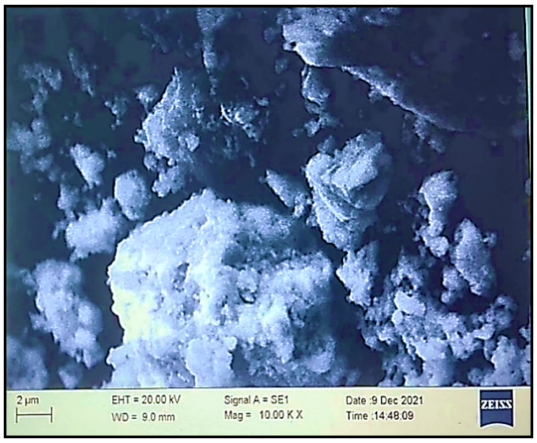

requirements of both XRD and FESEM analysis contribute to the majority of the variations in particle size. In the present case, the FESEM analysis shows a slightly larger particle size (37.5 nm) compared to the XRD analysis (34 nm), which could be due to the presence of agglomerates or aggregates that are not detected by XRD. The particle size obtained from XRD is an average value, which may not necessarily represent the actual particle size. On the other hand, FESEM analysis provides direct imaging of the particle morphology and size. It measures the physical size of the particles, which may include agglomerates or aggregates.

3.2.2. Difference between both techniques

XRD Analysis

1) Any powder sample's crystallite size, or the size of the coherent scattering domain, is measured by XRD.
2) XRD is more precise in revealing additional information regarding the material's lattice characteristics and crystal structure.
3) Crystallite size may be detected by XRD; however, aggregates or agglomerates cannot be detected.

FESEM (Field emission scanning electron microscopy) Analysis

1) FESEM measures the physical particle size of any powder sample.
2) Surface morphology may be detected more accurately by FESEM.
3) Agglomerates or aggregates may be detected by FESEM, which, in contrast to XRD, may result in larger particle sizes.

3.3. Thermoluminescence (TL) analysis

The occurrence in which a substance that has been heated emits light that has been previously stimulated is also referred to as TL. The long afterglow characteristics of thermoluminescent phosphor, also known as persistent luminescence, are extremely useful in many different applications. The TL features are very essential in an extensive variety of applications, like as monitoring of the environment, bioimaging in healthcare facilities, cancer detection, scintillation detectors, radiation detection, defense & measurement, dating archaeological evidence artifacts, geological sciences, and exposing food to radiation as security precautions. When the silicate material undergoes heating, its stored charges can be liberated in the form of energy, revealing important details regarding chronological age or exposure to radiation. Silicate materials possess significance for the reason that they are capable of being employed as TL materials, consisting of some glasses or ceramics. The different silicate materials have been widely investigated for their thermoluminescent properties for long-persistent behavior in the last few years [18].

3.3.1. Concentration effect of Dy^{3+} ions in TL intensity

The TL glow curve of UV-irradiated $Ba_2MgSi_2O_7$: Dy^{3+} sample containing 3 mol% concentration of dysprosium ions is shown in Figure 4 at different UV exposure time. The measurements were carried out a fixed heating rate 5 °C/s. It is readily apparent that the TL intensity rises on rising concentration of dopant [Dy^{3+}] ions, reaches its maximum at 3 mole%, and falls at higher concentrations of [Dy^{3+}] ions [11]. As the activator concentration rises, the distance between the activator ions reduces. The ion interaction improves, and it results in enhanced energy transfer. Conversely, a decrease in the activator concentration results in a decrease in the stored power of the ions. Consequently, the activator attains its optimal concentration. When the dopant level is raised more, the TL output steadily declines. It is the term adopted to describe this phenomenon of concentration. It may be proposed that the energy passes through one activator (donor) to a different recipient (acceptor) in order to be utilized [25]. A greater understanding of the precise mechanism leading to this concentration quenching effect requires addressing the critical distance (R_c) between the activator ion and the quenching ions [26].

3.3.2. Critical distance of energy transfer (R_c)

de Vries et al. [27] gave an important empirical formula for the calculation of the critical distance (R_c). Employing a specific mathematical formula [26, 27], we can figure out the critical distance (R_c), beyond which concentration quenching occurs, according to this hypothesis:

$$R_c = 2\left(\frac{3V}{4\pi X_c N}\right)^{\frac{1}{3}} \tag{5}$$

where X_c denotes the total critical concentration of dopant [Dy^{3+}] ions per unit cell, N denotes the number of cations in the unit cell, and V denotes the unit cell volume obtained from XRD patterns. For the $Ba_2MgSi_2O_7$:Dy^{3+} phosphor, according to the experimental and analytic values of V, N, and X_c (303.0, 4, 0.030), the critical distance (R_c) between Dy^{3+} ions in $Ba_2MgSi_2O_7$ is determined to be ~16.89 Å. In accordance with Dexter and Schulman's theory [28], the electric multipolar interaction mechanism (i.e., energy transfer process) or exchange interaction must play a role in controlling the concentration quenching in Dy^{3+}-activated $Ba_2MgSi_2O_7$. The three multipolar processes are widely recognized to be the dipole-dipole (d-d), dipole-quadrupole (d-q), and quadrupole-quadrupole interactions [26]. According to the de Vries et al.'s [27] theory, since the value of the critical distance (R_c) was not less than 5 Å, it can be argued on this basis that the exchange interaction was not solely for the concentration quenching and might be due to a non-radiative energy transfer process between one activator [Dy^{3+}] ion and another activator [Dy^{3+}] ion in the host crystal lattice site. If the critical distance exceeds 5 Å, it indicates that the concentration quenching in its host matrix is controlled by only a multipole-multipolar process [26, 27].

3.3.3. Electron or hole trap mechanism in synthesized $Ba_2MgSi_2O_7$: Dy^{3+} phosphor

In $Ba_2MgSi_2O_7$: Dy^{3+} phosphor, alkaline earth metal ions are capable to balance out (i.e., neutralize) the charge that is produced when Dy^{3+} ions are substituted for Ba^{2+} ions. As a result, it raises the luminescence intensity and stabilizes the crystal structure. The

Figure 4
TL glow curve of Dy^{3+}-doped $Ba_2MgSi_2O_7$ powder sample

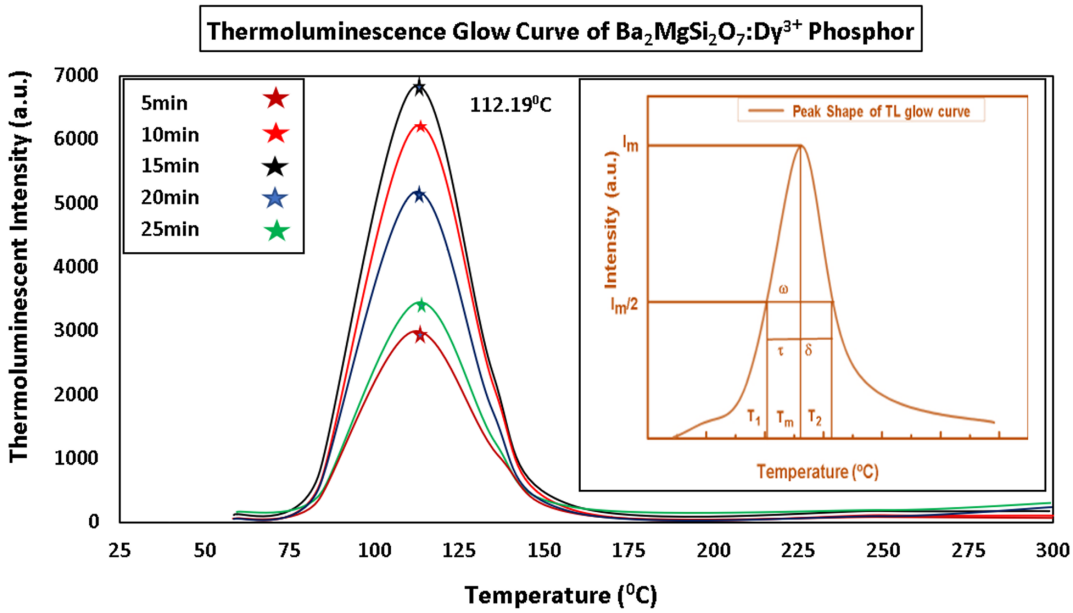

hole trap in alkaline earth is believed to be induced by ion vacancies, while the electron trap is most likely caused by trivalent dysprosium ions. The majority of the stimulation energy caused by excited charge carriers, like electrons or holes, will be transported from the host $Ba_2MgSi_2O_7$ lattice site towards the luminescence centers following the UV light irradiation in our experiment. Whenever some of the stimulated charge carriers fall into the traps and, instead of the shift to the ground state, a certain amount of the stimulation energy will remain conserved [11]. The emission coefficient becomes deeper over a longer duration of time whenever dopant [Dy^{3+}] ions are deliberately replaced for the Ba^{2+} ions in the host crystal lattice site ($Ba_2MgSi_2O_7$) through a doping process. In addition, two dopant [Dy^{3+}] ions appear to be able to take the place of three Ba^{2+} ions and stimulate the occurrence of dopant [Dy^{3+}] ion imperfections that serve as traps for electrons along with potential oxygen vacancies for the purpose of preserve the compound electroneutrality [15].

The following relation may be utilized to demonstrate the preceding process:

$$2Dy^{3+} + 3Ba^{2+} \rightarrow 2[Dy_{Ba}] * + [V_{Ba}]'' \quad (6)$$

Two positive defects [Dy_{Ba}]* attracting electrons and one negative vacancy [V_{Ba}]" would result from each replacement of two dopant [Dy^{3+}] ions. The charge carriers exploit these imperfections as capturing locations. This would result in the two [Dy_{Ba}]* defects serving as acceptors of electrons and the vacancy [V_{Ba}]" acting as the donor of electrons. The electrons that come out of the [V_{Ba}]" vacancies will subsequently be fully carried to the dopant [Dy^{3+}] lattice sites through thermal stimulation of any kind, as appears [15].

3.3.4. Calculation of kinetic or trapping parameters

Chen's [29] peak contouring approach is an appropriate method of experimentation for estimating the significance of kinetic parameters like activation energy [E], order of kinetics [b], and frequency factor [S] via the recognized TL glow peak of as-prepared powder samples. For various UV radiation periods of time, such as 5, 10, 15, 20, and 25 mins, the TL spectra of the $Ba_2MgSi_2O_7$: Dy^{3+} phosphor are shown in Figure 4. The present circumstance implies a rise in TL intensity of up to 15 min depending on the irradiation time, and, afterwards, it falls gradually as a consequence of the population's amount of trapped charge carriers attaining its maximum amount at a particular time in a metastable condition. It has been identified that it contains a single prominent peak at 112.19 °C on the TL glow curve. The order of kinetics [b] refers to the recombination process of de-trapped charge carriers with their corresponding counterparts. This trapping parameter may be figured out via calculating shape factor (μ_g) from the mathematical relation as follows:

$$\mu_g = \frac{\delta}{\omega} = \frac{T_2 - T_m}{T_2 - T_1} \quad (7)$$

where T_m symbolizes the optimum temperature, and T_1 and T_2 symbolize the temperatures at half intensity on the ascending and descending parts of the TL glow peak curve, respectively, [$\omega = T_2 – T_1$], the optimum-temperature half width [$\delta = T_2 – T_m$] maxima (FWHM). Remarkably, the shape factor (μ_g), spanning from 0.49 to 0.50, is about the value of the second-order kinetics [i.e., $\mu_g = 0.49–0.52$]. As a result, enhancing the probabilities of re-trapping released carriers of charges immediately prior to the to the beginning of the recombination mechanism. For the purpose of determining the value of trap depth (E)/activation energy, we utilized the aforementioned formula [18, 29]:

$$E_\alpha = C_\alpha \left(\frac{kT_m^2}{\alpha}\right) - b_\alpha (2kT_m) \quad (8)$$

where the Boltzmann constant is denoted by k. This mathematical equation provides the relationship between the depth of the trap (E)/activation energy and the frequency factor (s):

Table 2
TL kinetic or trapping parameters of prepared $Ba_2MgSi_2O_7$: Dy^{3+} powder sample

UV exposure time (in min)	Peak temperature T_m (°C)	Trap depth E (eV)	Frequency factor (S/s)
5 min	112.19	0.66	1.1×10^7
10 min	112.19	0.74	1.3×10^7
15 min	112.19	0.73	1.3×10^7
20 min	112.19	0.73	1.3×10^7
25 min	112.19	0.70	1.2×10^7

$$\frac{\beta E}{kT_m^2} = s\left[1 + (b-1)\frac{2kT_m}{E}\right]\exp(-E/kT_m) \quad (9)$$

where *b* symbolizes the order of the kinetics, that is, the value is equal to two in the present case, and β is the rate of heating.

The trapping parameters derived by the Chen [29] glow curve method regarding the $Ba_2MgSi_2O_7$: Dy^{3+} phosphor are listed in Table 2. Correspondingly, the frequency factor (s^{-1}) was calculated to be in the range of (1.1×10^7 to 1.3×10^7 s^{-1}). The range of values of 0.66 to 0.74 eV is determined for trap depth or activation energy, indicating that the sample shows an increased amount of persistency with regard to its TL characteristics. It is in accordance with the reports that the materials demonstrate long persistence properties at a value of depth of trap/activation energy (E) spanning between 0.65 and 0.75 eV [18, 30]. As a result, deeper traps are highly beneficial for extending afterglow durations and a long-term persistency for completely releasing captured holes or electrons. As a result, dopant [Dy^{3+}] ion generates deeper traps in host lattice crystal site. Because the defect level formed by Dy^{3+} ions is deeper. Deeper traps can enhance the stability of the luminescent centers, preventing them from deactivating quickly and thereby increasing the afterglow duration and persistence, allowing for more light emission.

3.4. Photoluminescence (PL) spectral analysis

3.4.1. Excitation and emission spectra

The optical properties (PL) including excitation and emission spectrum of $Ba_2MgSi_2O_7$: Dy^{3+} phosphor with 3 mol% doping concentrations are shown in Figure 5(a) and (b). It is obvious that the peak of both excitation and emission spectra is definitely located at the wavelength, where the largest amount of luminescence intensity was obtained at a doping concentration of 3 mol%. The excitation bands at 335, 353, and 385 nm correspond to the transitions from the $^6H_{15/2}$ ground state to the excited states $^6P_{3/2}$, $^6P_{7/2}$, and $^4P_{13/2}$, respectively [30, 31]. Among the bands, 353 nm is the most intense, and it corresponds to the transition $^6H_{15/2} \rightarrow {}^6P_{7/2}$ [32] and is employed as the excitation wavelength. In addition to causing the extremely dense and overlapping levels of the $^4f_9$ electronic configuration of the dopant [Dy^{3+}] ions in the high energy region. These spectral lines are also held accountable for the transitions from low energy states to high energy states in the intra-configurational (4f–4f) transitions [18].

The UV radiation source working at 353 nm is recommended to be employed to stimulate the sintered phosphor. Dysprosium (Dy^{3+}) plays the most significant role in synthesizing materials capable of white light emissions. With the addition of Dy^{3+} ions, three prominent emission bands in the red, yellow, and blue regions are expected to occur. In Figure 5(b), there are three prominent peaks in the visible region situated at 474 nm, 572 nm, and 667 nm owing to transitions: $^4F_{9/2} \rightarrow {}^6H_{15/2}$ (blue), $^4F_{9/2} \rightarrow {}^6H_{13/2}$ (yellow), and $^4F_{9/2} \rightarrow {}^6H_{11/2}$ (red), respectively [16, 33]. It is established that the magnetic dipole [$^4F_{9/2} \rightarrow {}^6H_{15/2}$] transition is correlated with Dy^{3+} emission at 474 nm (blue), while the electric dipole [$^4F_{9/2} \rightarrow {}^6H_{13/2}$] transition is correlated with emission at 572 nm (yellow)], as well as the magnetic dipole [$^4F_{9/2} \rightarrow {}^6H_{11/2}$] transition is correlated with Dy^{3+} emission at 667 nm (red) [34]. The magnetic dipole transition $^4F_{9/2} \rightarrow {}^6H_{15/2}$ is mostly insensitive to the strength of the crystal field surrounding the Dy^{3+} ions [35].

According to Judd-Ofelt theory [15], the $^4F_{9/2} \rightarrow {}^6H_{13/2}$ transition corresponds to a strong electric dipole transition ($\Delta L = 2$; $\Delta J = 2$) and a hypersensitive transition of Dy^{3+} ions. This hypersensitive transition is highly dependent on the surrounding environment for an inferior symmetrical lattice lacking an inversion center [36] through modifying the magnitude of the integrated intensity ratio of yellow to blue (Y/B). When Dy^{3+} ions occupy the lower symmetry sites, the corresponding Y/B intensity ratio becomes greater than 1, and vice versa. The ratio of yellow to blue (Y/B) is referred to as an asymmetric ratio (I). Usually, the asymmetric ratio (I) of the electric dipole transition (572 nm) to the magnetic dipole transition (474 nm) is an indication of the symmetry direction of the local environment around the Dy^{3+} ion site [17]. The presence of highly

Figure 5
(a) Excitation spectrum of Dy^{3+}-activated $Ba_2MgSi_2O_7$ powder sample (b) Emission spectrum of Dy^{3+}-activated $Ba_2MgSi_2O_7$ powder sample

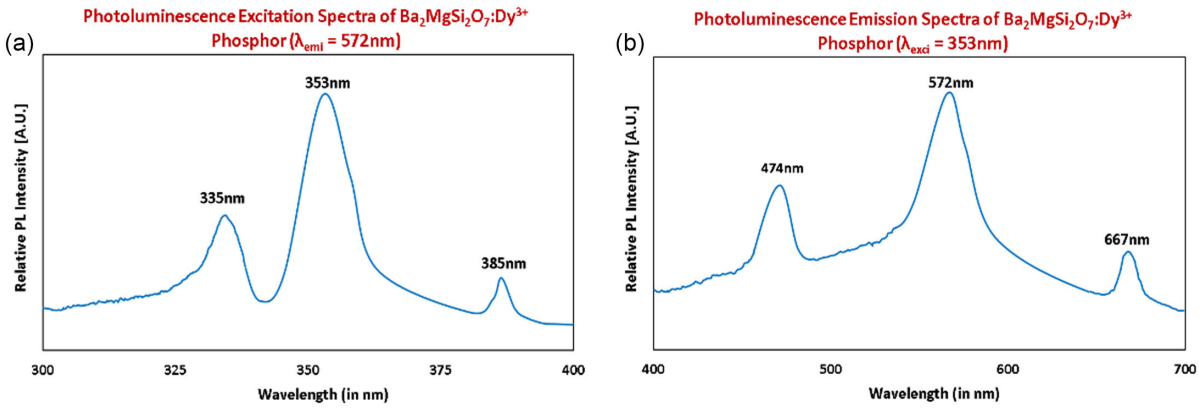

asymmetric coordination environments enhances the emission properties of Dy^{3+} ions. The intensified photoemission is primarily attributed to enhanced energy transfer processes and an increased probability of radiative transitions.

3.4.2. The effects of asymmetric ratio (I) in crystal field splitting

It is very clear that the asymmetric ratio affects the crystal field splitting and the distribution of energy levels within the 4f shell of Dy^{3+} ions. This, in turn, influences the absorption and emission wavelengths of the ions. The increased asymmetry in the coordination environment leads to more efficient energy transfer between neighboring ions, promoting the population of excited states. This can lead to an enhancement of the radiative emission. Overall, the asymmetric ration plays a crucial role in influencing the energy transfer processes, crystal field splitting, and radiative transition probabilities, ultimately intensifying the photoemission surrounding the environment of Dy^{3+} ions. The unique properties of Dy^{3+} ions, including high quantum efficiency, broad absorption and emission bands, as well as long excited-state lifetimes, contribute to their superior emission efficiency in SSL compared to other materials.

In the situation, wherein Dy^{3+} ions are located to the low-symmetry sites, the $^4F_{9/2} \rightarrow {}^6H_{13/2}$ transition has an enhanced emission intensity in comparison to the $^4F_{9/2} \rightarrow {}^6H_{15/2}$ transition [31]. Because of an electric dipole transition, which is only possible when Dy^{3+} ions are located at low-symmetry sites and where no inversion centers are present, the Y/B ratio is frequently utilized to observe the in-situ environment of the Dy^{3+} ions in each host matrix [12]. It may be feasible to utilize Dy^{3+}-doped luminophores for producing white light by adjusting the asymmetric ratio (I) of yellow to blue (Y/B) emission intensities [37]. The luminescence intensity has been revealed to be dependent on the environment around the diverging crystal fields. Whereas the transition ($^4F_{9/2} \rightarrow {}^6H_{15/2}$) is less host-sensitive.

3.4.3. Effect of the color temperature

However, it is clearly evident from the PL emission spectra of synthesized material that the yellow emission becomes predominant compared to the blue emission, which suggests that the dopant [Dy^{3+}] ion is located in an antisymmetric site with a non-inversion center of the host matrix [38]. The color temperature is raised by the blue emission. Conversely, the stronger yellow emission decreases the color temperature. An essential aspect that comes out of both color combinations is the emission of white light. The red emission lines in the phosphor are extremely weak in comparison to the blue and yellow emission lines, which are both highly strong, intense, and sharp. In other words, it is obvious that red light emission has absolutely no impact on white light emission. The intensity of red emissions is noticeably lower in this instance than the intensity of blue and yellow emissions. The result indicates that, as the temperature at which the calcination occurs increases, the alteration of the positioning site symmetry around the dopant [Dy^{3+}] ions causes an increase in the ratio of yellow to blue color emission (Y/B).

3.4.4. What is the dysprosium (Dy) content in this $Ba_2MgSi_2O_7$: Dy^{3+} sample?

The modern periodic table contains the rare-earth element dysprosium, which emits white light when doped with any inorganic compound. Its atomic number is 66, and its symbol is "Dy". It may be frequently employed in a variety of minerals & materials due to its special optical and magnetic properties. The dysprosium ion has a +3 charge, which is its most common oxidation state. However, to determine the exact dysprosium content in the synthesized compound ($Ba_2MgSi_2O_7$: Dy^{3+}), you would need to know specific concentration details about the sample. In the present research work, the dysprosium content in the $Ba_2MgSi_2O_7$:Dy^{3+} phosphor sample is 3 mol% concentration. The luminescence intensity rises with a rising concentration of dopant [Dy^{3+}] ions, reaches its optimum at 3 mol%, and falls at higher concentrations of [Dy^{3+}] ions due to concentration quenching.

3.5. Photometric characterization

3.5.1. CIE chromaticity coordinates

Examining the phosphor practical applications requires an understanding of the color chromaticity features. The CIE chromaticity coordinates of the Dy^{3+}-activated $Ba_2MgSi_2O_7$ phosphor were computed with the help of the CIE 1931 chromaticity software, as readily shown in Figure 6, on the basis of the photoluminescence (PL) emission spectrum [14, 15, 24]. The standard chromaticity coordinates for the emission of conventional white light are $x = 0.3333$ and $y = 0.3333$. The CIE coordinates for the as-synthesized phosphor are $x = 0.32$ and $y = 0.33$, which exactly match the standard CIE coordinates for the production of w-LEDs. Trivalent rare-earth (RE^{3+}) ions are vital for the generation of illuminated materials exhibiting high efficiency [39]. It is generally agreed that when an inorganic material is doped with Dy^{3+} ions, it is responsible for white light emission. Similarly, with this possibility, when a glass host matrix is doped with Dy^{3+} ions, it is equally responsible for producing the w-LEDs [40]. The (x, y) coordinates are obviously pointed in the direction of the spot that emits white light, which produces prominent blue and yellow light emissions, and could potentially be preferred after considering the findings reported above. Because the color temperature is raised by the blue emission, and the strong yellow emission also decreases the color temperature. Both color combinations are responsible for white light emission.

3.5.2. CCT

The Mc Camy empirical formula was used to estimate the CCT with the help of the evaluated CIE chromaticity coordinates [41]:

$$CCT = -437n^3 + 3601n^2 - 6861n + 5514.31 \quad (10)$$

Figure 6
CIE diagram of Dy^{3+}-activated $Ba_2MgSi_2O_7$ powder sample

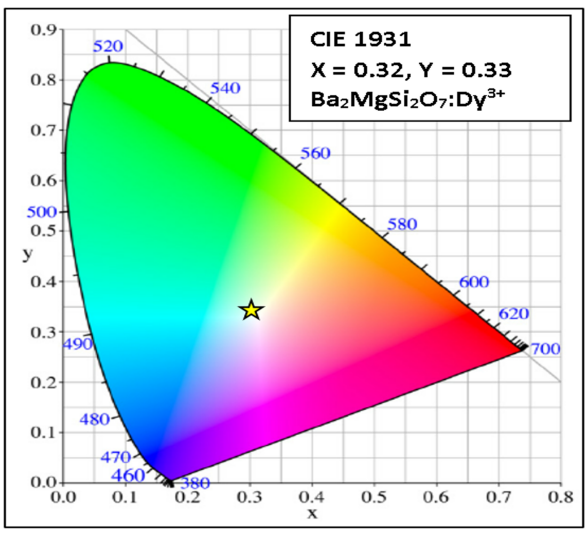

where $n = \frac{(x - x_c)}{(y - y_c)}$ via 1931 x–y chromaticity figures [40–43]. Usually, the correlated color temperature (CCT) of a light source is independent of its temperature and the values are in the ranges: [a] (2700–3000 k) for warm light emission, [b] (3000–4000 k) for neutral light emission and [c] (4000–6500 k) for cool light emission [43]. The results clearly indicated that the as-synthesized phosphor might be suitable for the generation of white light emission. The calculated CCT of Dy^{3+}-activated $Ba_2MgSi_2O_7$ phosphor was found to be 6113 K, which falls in the cool light color temperature range. A strong color rendering index R_a exceeding 89 was also displayed. CCT and CRI are more appropriate for producing white light emissions. The CIE parameters of Dy^{3+}-activated $Ba_2MgSi_2O_7$ phosphor are represented in Table 3.

Table 3
The CIE parameters of Dy^{3+}-activated $Ba_2MgSi_2O_7$ phosphor

	Color coordinates			
xDy	x	y	CCT (K)	Color rendering index (R_a)
3 mol%	0.32	0.33	6113	89

Currently, material scientists and researchers are working on developing a system for a new conventional phosphor that can emit full white light by doping with single activator ions. So, it can be used in white SSL devices. However, very few reports confirm that we can obtain full-color-emitting phosphors from single-doped activator ions. To achieve the full-color emission of white light, the precision of the emission point of the CIE coordinates can be substantially adjusted by variations in the composition value of the asymmetric ratio (i.e., Y/B emission intensity). Therefore, the synthesized Dy^{3+}-activated $Ba_2MgSi_2O_7$ phosphor is committed to producing full white light emission.

4. Conclusion

In summary, Dy^{3+}-activated $Ba_2MgSi_2O_7$ nanocrystalline phosphor was successfully synthesized using the conventional combustion synthesis technique and further characterized by employing of XRD, FESEM, PL, CIE, and TL analysis. XRD pattern confirms the pure single-phase state and monoclinic structure of the host ($Ba_2MgSi_2O_7$) in the space group of C2/c. The agglomerated particles possessing a flake-like arrangement, uniformity, homogeneity, and variety of grain sizes in the nanometers range are apparent. Strong hypertensive electronic transitions ($^4F_{9/2} \rightarrow {}^6H_{15/2,\ 13/2,\ 11/2}$) of Dy^{3+} ions have been attributed to the emission spectral peaks at 474 nm (blue), 572 nm (yellow), and 667 nm (red) in the PL emission spectrum. In our investigation, the critical distance (R_c) is calculated as 16.89 Å; therefore, the mechanism involved in the concentration quenching of $Ba_2MgSi_2O_7$ doped with 3.0 mol% of Dy^{3+} ions are considered to be the multipole-multipolar interaction. The synthesized nanophosphor has been determined to possess a value of CIE chromaticity coordinate of (x = 0.32, y = 0.33), CCT 6113 K, and a strong color rendering index (R_a) exceeding 89, which produces cool illumination in the white color region. In TL analysis, single and intense broadband glow peak was observed at 112.19 °C. The probability of liberated charge carriers could potentially be re-trapped prior to recombination, as is supported by second-order kinetics. It becomes apparent that the value of trap depth/activation energy ranges from 0.66 to 0.74 eV for UV exposure time between 10 min and 25 min, respectively. Consequently, deeper traps are highly beneficial for extending the afterglow process and its long-term persistency. With the majority of the samples created, the white afterglow can persist for an hour, indicating potential candidates for the production of white LED-based SSL devices. Considering an outstanding candidate of more effective thermoluminescent material and white extended afterglow phosphor.

5. Potential Application in Various Fields

The enhanced emission properties of Dy^{3+} ions in their surrounding environment have potential practical application in various fields. Their unique characteristics make them valuable in diverse fields and contributing to advancements in technology, energy efficiency, healthcare, nanotechnology, plasma display panels (PDPs), WLED-based SSL devices, security features, magnetic resonance imaging (MRI), efficient and high-performance devices for communication, optical fibers, sensing, lasers, optoelectronics, and energy storage devices. As well as considering the scope of this area of long-persistent phosphor (LPP) and thermoluminescent material for radiation dosimetry, personnel, and environmental monitoring applications.

Acknowledgement

Both authors are greatly acknowledged to Dept. of Physics, Dr. Radha Bai, Govt. Navin Girls College, Raipur (C.G.), for sample preparation, and Pt. Ravishankar Shukla University, & NIT Raipur (C.G.), India, were supported for the sample characterization facilities by the collaboration. This present research is based on unpublished research data from the Ph.D. degree of Dr. Sanjay Kumar Dubey (2018–2022).

Ethical Statement

This study does not contain any studies with human or animal subjects performed by any of the authors.

Conflicts of Interest

The authors declare that they have no conflicts of interest to this work.

Data Availability Statement

Data sharing is not applicable to this article as no new data were created or analyzed in this study.

Author Contribution Statement

Shashank Sharma: Conceptualization, Methodology, Validation, Formal analysis, Investigation, Resources, Data curation, Writing – original draft, Writing – review & editing, Visualization, Supervision. **Sanjay Kumar Dubey:** Conceptualization, Methodology, Validation, Formal analysis, Investigation, Resources, Data curation, Writing – original draft, Writing – review & editing, Visualization, Supervision.

References

[1] Reshak, A. H., Alahmed, Z. A., Bila, J., Atuchin, V. V., Bazarov, B. G., Chimitova, O. D., . . . , & Yelisseyev, A. P. (2016). Exploration of the electronic structure of monoclinic α-Eu_2 $(MoO_4)_3$: DFT-based study and X-ray photoelectron spectroscopy. *The Journal of Physical Chemistry C*, *120*(19), 10559–10568. https://doi.org/10.1021/acs.jpcc.6b01489

[2] Xia, Z., Zhang, Y., Molokeev, M. S., Atuchin, V. V., & Luo, Y. (2013). Linear structural evolution induced tunable photoluminescence in clinopyroxene solid-solution phosphors. *Scientific Reports*, *3*(1), 3310. https://doi.org/10.1038/srep03310

[3] Annadurai, G., Masilla Moses Kennedy, S., & Sivakumar, V. (2018). Synthesis of novel Dy^{3+} activated $Ba_2CaZn_2Si_6O_{17}$ phosphors for white light-emitting diodes. *Luminescence*, *33*(3), 521–527. https://doi.org/10.1002/bio.3441

[4] Cao, R., Lv, X., Jiao, Y., Ran, Y., Guo, S., Ao, H., . . . , & Fan, T. (2020). $Ca_3La_6Si_6O_{24}$: Eu^{3+} orange-red-emitting phosphor: Synthesis, structure and luminescence properties. *Materials Research Bulletin*, *122*, 110651. https://doi.org/10.1016/j.materresbull.2019.110651

[5] Mayavan, A., Ganesamurthi, J. S., Jang, K., & Gandhi, S. (2021). Development of bluish green-emitting $Ca_{2-x}Eu_xSiO_4$ phosphor: A novel approach using silica nanoparticles as precursor. *Journal of Luminescence*, *230*, 117664. https://doi.org/10.1016/j.jlumin.2020.117664

[6] Deng, B., Chen, J., Zhou, C., Zeng, F., & Liu, H. (2020). Improved near-IR emission in Yb^{3+}-condensed fluorosilicate apatite $Sr_4Yb_6(SiO_4)_6F_2$ via Eu^{3+} doping. *Journal of Luminescence*, *225*, 117355. https://doi.org/10.1016/j.jlumin.2020.117355

[7] Bhure, P. P., Puppalwar, S. P., Tingane, K. T., Sahu, K. V., Suryawanshi, S. M., & Bahirwar, B. M. (2023). Luminescence properties of Eu^{3+} doped Li_2SrSiO_4 phosphor. In *IOP Conference Series: Earth and Environmental Science, 1281*(1), 012041. https://doi.org/10.1088/1755-1315/1281/1/012041

[8] Alajlani, Y., Oglakci, M., Kaynar, U. H., Ayvacikli, M., Portakal-Uçar, Z. G., Topaksu, M., & Can, N. (2021). Thermoluminescence study and evaluation of trapping parameters of samarium doped barium silicate phosphor. *Journal of Asian Ceramic Societies*, *9*(1), 291–303. https://doi.org/10.1080/21870764.2020.1864898

[9] Chen, X., Li, H., Zhang, P., Xiang, R., & Li, G. (2021). Phase composition, microstructure, and microwave dielectric properties of $CaMnSi_2O_6$ ceramics. *Ceramics International*, *47*(3), 4083–4089. https://doi.org/10.1016/j.ceramint.2020.09.282

[10] Dubey, S. K., Sharma, S., Diwakar, A. K., & Pandey, S. (2021). Synthesization of monoclinic ($Ba_2MgSi_2O_7$: Dy^{3+}) structure by combustion route. *Journal of Materials Science Research and Reviews*, *4*(4), 595–602.

[11] Wang, Q. Y., Yuan, P., Wang, T. W., Yin, Z. Q., & Lu, F. C. (2020). Effect of Sr and Ca substitution of Ba on the photoluminescence properties of the Eu^{2+} activated $Ba_2MgSi_2O_7$ phosphor. *Ceramics International*, *46*(2), 1374–1382. https://doi.org/10.1016/j.ceramint.2019.09.100

[12] Bedyal, A. K., Kunti, A. K., Kumar, V., & Swart, H. C. (2019). Effects of cationic substitution on the luminescence behavior of Dy^{3+} doped orthophosphate phosphor. *Journal of Alloys and Compounds*, *806*, 1127–1137. https://doi.org/10.1016/j.jallcom.2019.07.305

[13] Park, J. Y., Park, S. J., Moon, B. K., Kwak, M., Jang, K., & Yang, H. K. (2018). High temperature synthesis of yellow-emitting $Y_2BaAl_4SiO_{12}$: Ce^{3+} phosphors for WLED applications. *Chemical Physics Letters*, *708*, 66–70. https://doi.org/10.1016/j.cplett.2018.08.003

[14] Bharathi, N. V., Kavitha, P., Ramaswamy, S., Jayabalakrishnan, S. S., & Sakthipandi, K. (2022). Turning of luminescence properties of $Ba_2V_2O_7$ phosphors by co-doping Eu^{3+}/Dy^{3+} ions. *Bulletin of Materials Science*, *45*(3), 172. https://doi.org/10.1007/s12034-022-02741-1

[15] Sharma, S., & Dubey, S. K. (2022). Importance of the color temperature in cold white light emission of $Ca_2MgSi_2O_7$: Dy^{3+} phosphor. *Journal of Applied Chemical Science International*, *13*(4), 80–90. https://doi.org/10.56557/jacsi/2022/v13i47769

[16] Revannasiddappa, G. R., Basavaraj, R. B., Rudresha, M. S., Nagaraju, G., Kumar, S., & Sasidhar, N. (2021). White-light emitting $Ca_2MgSi_2O_7$: Dy^{3+} nanopowders: Structural, spectroscopic investigations and advanced forensic applications. *Vacuum*, *184*, 109940. https://doi.org/10.1016/j.vacuum.2020.109940

[17] Verma, S., Kumar, D., Dutta, S., Sharma, V., Swart, H. C., & Kumar, V. (2020). A novel near white light emitting phosphor $KSrYSi_2O_7$: Dy^{3+}: Synthesis, characterization and luminescence properties. *Vacuum*, *174*, 109179. https://doi.org/10.1016/j.vacuum.2020.109179

[18] Sharma, S., & Dubey, S. K. (2023). Enhanced thermoluminescence properties of synthesized monoclinic crystal structure. *Global Journal of Materials Science and Engineering*, *5*(1), 146.

[19] Parauha, Y. R., Sahu, V., & Dhoble, S. J. (2021). Prospective of combustion method for preparation of nanomaterials: A challenge. *Materials Science and Engineering: B*, *267*, 115054. https://doi.org/10.1016/j.mseb.2021.115054

[20] Liu, G., Chen, K., & Li, J. (2018). Combustion synthesis: An effective tool for preparing inorganic materials. *Scripta Materialia*, *157*, 167–173. https://doi.org/10.1016/j.scriptamat.2018.08.022

[21] Zhang, X., Zhang, J., Wang, R., & Gong, M. (2010). Photo-physical behaviors of efficient green phosphor $Ba_2MgSi_2O_7$: Eu^{2+} and its application in light-emitting diodes. *Journal of the American Ceramic Society*, *93*(5), 1368–1371. https://doi.org/10.1111/j.1551-2916.2009.03549.x

[22] Mondal, K., & Manam, J. (2020). Colour-tunable luminescence and thermal stability of blue-green emitting $Ba_2MgSi_2O_7$: Ce^{3+}, Tb^{3+} phosphors. *Journal of Molecular Structure*, *1215*, 128262. https://doi.org/10.1016/j.molstruc.2020.128262

[23] Shannon, R. D. (1976). Revised effective ionic radii and systematic studies of interatomic distances in halides and chalcogenides. *Acta Crystallographica Section A: Foundations and Advances*, *32*(5), 751–767. https://doi.org/10.1107/S0567739476001551

[24] Lim, C. S., Aleksandrovsky, A., Molokeev, M., Oreshonkov, A., & Atuchin, V. (2021). Structural and spectroscopic effects of Li^+ substitution for Na^+ in $Li_xNa_{1-x}CaGd_{0.5}Ho_{0.05}Yb_{0.45}(MoO_4)_3$ scheelite-type upconversion phosphors. *Molecules*, *26*(23), 7357. https://doi.org/10.3390/molecules26237357

[25] Bos, A. J. J. (2017). Thermoluminescence as a research tool to investigate luminescence mechanisms. *Materials*, *10*(12), 1357. https://doi.org/10.3390/ma10121357

[26] Golja, D. R., & Dejene, F. B. (2020). Effect of Eu^{3+} ion concentration on the structural and photoluminescence properties of $Ba_{1.3}Ca_{0.7}SiO_4$ ceramic-based red phosphors for solid-state lighting applications. *Journal of Alloys and Compounds*, *827*, 154216. https://doi.org/10.1016/j.jallcom.2020.154216

[27] de Vries, A. J., Minks, B. P., & Blasse, G. (1988). Evaluation of the energy migration in $GdAl_3B_4O_{12}$. *Journal of Luminescence*, *39*(3), 153–160. https://doi.org/10.1016/0022-2313(88)90070-1

[28] Dexter, D. L., & Schulman, J. H. (1954). Theory of concentration quenching in inorganic phosphors. *The Journal of Chemical Physics, 22*(6), 1063–1070. https://doi.org/10.1063/1.1740265

[29] Chen, R. (1969). Glow curves with general order kinetics. *Journal of the Electrochemical Society*, *116*(9), 1254. https://doi.org/10.1149/1.2412291

[30] Mashangva, M., Singh, M. N., & Singh, T. B. (2011). Estimation of optimal trapping parameters relevant to persistent luminescence. *Indian Journal of Pure & Applied Physics*, *49*, 583–589.

[31] Douzi, A., Slimi, S., Madirov, E., Turshatov, A., Richards, B. S., Solé, R. M., …, & Mateos, X. (2023). Structure and luminescence properties of Dy^{3+} doped quaternary tungstate $Li_3Ba_2Gd_3(WO_4)_8$ for application in wLEDs. *RSC Advances*, *13*(34), 23772–23787. https://doi.org/10.1039/D3RA02501B

[32] Kumar, K. G., Bhargav, P. B., Aravinth, K., Arumugam, R., & Ramasamy, P. (2020). Dysprosium activated strontium aluminate phosphor: A potential candidate for WLED applications. *Journal of Luminescence*, *223*, 117126. https://doi.org/10.1016/j.jlumin.2020.117126

[33] Kohale, R. L., Utane, R., & Dhoble, S. J. (2021). Synthesis and characterization of Dy^{3+} activated $Ca_2Al_2SiO_7$ nanophosphors for environment friendly lighting. *International Journal of Scientific Research in Science and Technology*, *8*(1), 42–45.

[34] Bhelave, S. R., Yerpude, A. N., Panse, V. R., Saregar, A., & Dhoble, S. J. (2023). Study the photoluminescence properties of $Ca_4Al_{14}O_{25}$: Dy^{3+} phosphor for solid state lighting. In *AIP Conference Proceedings, 2595*(1), 030003. https://doi.org/10.1063/5.0123776

[35] Tatte, S. P., Dhoble, N. S., Mishra, G. C., & Dhoble, S. J. (2022). Synthesis characterization and luminescence properties of $B_2BiMg_2V_3O_{12}$ based phosphors with rare earth activated Dy^{3+} phosphor for solid state lighting. *IOP Conference Series: Materials Science and Engineering, 1258*(1), 012016. https://doi.org/10.1088/1757-899X/1258/1/012016

[36] Malik, C., Kaur, N., Singh, B., & Pandey, A. (2020). Luminescence properties of tricalcium phosphate doped with dysprosium. *Applied Radiation and Isotopes*, *158*, 109062. https://doi.org/10.1016/j.apradiso.2020.109062

[37] Liu, Q., Guo, J., Fan, M., Zhang, Q., Liu, S., Wong, K. L., …, & Wei, B. (2020). Fast synthesis of Dy^{3+} and Tm^{3+} co-doped double perovskite $NaLaMgWO_6$: A thermally stable single-phase white-emitting phosphor for WLEDs. *Journal of Materials Chemistry C*, *8*(6), 2117–2122. https://doi.org/10.1039/C9TC05592D

[38] Mahajan, R., Prakash, R., Kumar, S., Kumar, V., Choudhary, R. J., & Phase, D. M. (2021). Surface and luminescent properties of $Mg_3(PO_4)_2$:Dy^{3+} phosphors. *Optik*, *225*, 165717. https://doi.org/10.1016/j.ijleo.2020.165717

[39] Hussain, N., Rubab, S., & Kumar, V. (2023). Spectroscopic characterizations and investigation of Judd-Ofelt intensity parameters of Dy^{3+}-doped $Ba_2La_8(SiO_4)_6O_2$ near white light emitting phosphor. *Ceramics International*, *49*(10), 15341–15348. https://doi.org/10.1016/j.ceramint.2023.01.118

[40] Mbule, P., Mlotswa, D., Mothudi, B., & Dhlamini, M. (2021). Photoluminescence and thermoluminescence analysis of Zn_2SiO_4:Dy^{3+} nanophosphor. *Journal of Luminescence*, *235*, 118060. https://doi.org/10.1016/j.jlumin.2021.118060

[41] McCamy, C. S. (1992). Correlated color temperature as an explicit function of chromaticity coordinates. *Color Research and Application*, *17*(2), 142–144. https://doi.org/10.1002/col.5080170211

[42] Malik, C., Meena, R. K., Rathi, P., Singh, B., & Pandey, A. (2020). Effect of dopant concentration on luminescence properties of a phosphor $KCaPO_4$: Dy. *Radiation Physics and Chemistry*, *168*, 108561. https://doi.org/10.1016/j.radphyschem.2019.108561

[43] Jamalaiah, B. C., & Khan, P. S. (2023). $Sr_3Gd(PO_4)_3$: Dy^{3+} phosphors for lighting applications. *Journal of Sol-Gel Science and Technology*, *105*(1), 266–277. https://doi.org/10.1007/s10971-022-05995-7

How to Cite: Sharma, S., & Dubey, S. K. (2025). Study of Combustion-Derived Monoclinic Crystal ($Ba_2MgSi_2O_7$) Structure and Dy^{3+} Luminescence for Generation of White Long Afterglow Phosphor and Its Applications. *Journal of Optics and Photonics Research*, *2*(2), 93–103. https://doi.org/10.47852/bonviewJOPR42022592